The Dynamics of Error Growth and Predictability in a Model of the Gulf Stream. Part I: Singular Vector Analysis

ANDREW M. MOORE

Program in Atmospheric and Oceanic Sciences, and Cooperative Institute for Research in Environmental Sciences, University of Colorado, Boulder, Colorado

ARTHUR J. MARIANO

Department of Meteorology and Physical Oceanography, Rosenstiel School of Marine and Atmospheric Science, University of Miami, Miami, Florida

(Manuscript received 14 April 1997, in final form 2 February 1998)

ABSTRACT

The recently developed ideas of generalized linear stability theory for dynamical systems are applied to time evolving flows of the Gulf Stream using a quasigeostrophic numerical model. The potential for the growth of perturbations arising from errors and uncertainties in forecasts of the Gulf Stream is investigated by computing the singular vectors, or so-called optimal perturbations, of time evolving flows using a linearized model and its adjoint. The authors' calculations reveal that the potential for rapid perturbation growth is greatest in regions of developing straining and shearing flows. Such regions include developing meanders and regions where eddies form and where existing eddies interact with the main Gulf Stream. It is found that the optimal perturbations of the Gulf Stream share many features in common with those of the jet streams in the atmosphere. The ideas and techniques developed in this paper have been applied to the problem of ensemble prediction of the Gulf Stream in Part II.

1. Introduction

In recent years there has been an increasing interest in the prediction of ocean currents and the ocean circulation. These efforts have focused primarily on coastal and nearshore circulations because of their impact on marine operations and fisheries.

In meteorology, numerical weather prediction (NWP) techniques have evolved rapidly during the last 30 years or so, and much of the experience gained in NWP is directly applicable to ocean prediction. Based on the experience of NWP the quality or skill of an ocean forecast is likely to depend on a number of factors, which include the accuracy of the forecast model and the boundary condition data used to drive it as well as the accuracy of the observations and the integrity of the analysis procedure used to construct the initial conditions for the forecast. For nonlinear systems, an additional factor that will ultimately limit the predictability of the ocean is the stability of the circulation that is being forecast in the presence of perturbations arising from errors or uncertainties in the model initial and boundary conditions. If two nonlinear model forecasts are made starting from slightly different initial conditions (or using forcing fields or boundary conditions that differ), the forecasts will diverge in time and become increasingly dissimilar. The rate at which this occurs will depend upon the dynamical characteristics of the flow fields in the model. If we think of one of the forecasts as representing the real ocean and the other as representing our best forecast of the real ocean, then it is clear that the presence of uncertainties in the initial conditions (no matter how small) will limit the predictability of the ocean.

Traditionally, the stability of dynamical flow fields, such as those in the atmosphere and ocean, to small perturbations is assessed using the ideas of Raleigh (1880) in which growing perturbations, so-called normal modes, are sought that are characterized by exponential growth. If no growing normal modes exist, the flow is usually assumed to be stable. However, since the time of Kelvin (1887) and Orr (1907) it has been known that unstable flows exist that do not possess growing exponential normal modes. Recently, normal mode theory has been challenged (e.g., Farrell and Ioannou 1996a,b), and ideas about the stability of flows have been reformed by the observation that perturbation growth is more of-

Corresponding author address: Dr. Andrew M. Moore, Program in Atmospheric and Oceanic Sciences, University of Colorado, Campus Box 311, Boulder, CO 80309-0311.
E-mail: andy@australis.colorado.edu

ten than not initially characterized by rapid transient growth, not gradual exponential growth, and that such transient growth can occur in the absence of growing normal modes.

Despite the name given to them, the normal modes of most dynamical systems of interest are not orthogonal to one another. This means that it is possible to superimpose the normal modes of the system to produce perturbations that, during a finite time interval, can grow more rapidly than the most unstable normal mode. The disparity between the rate of growth of such a perturbation and the normal modes can be large (several orders of magnitude), and rapid transient growth is possible even when all the normal modes are stable. These ideas are fast gaining merit and have proved particularly useful for understanding the predictability of the atmosphere and coupled ocean–atmosphere system (e.g., Lorenz 1965; Lacarra and Talagrand 1988; Farrell 1990; Molteni and Palmer 1993; Mureau et al. 1993; Buizza et al. 1995; Moore and Kleeman 1996, 1997a,b, 1998, 1999; Molteni et al. 1996).

In relation to ocean forecasting, there has in recent years been a considerable effort to model and predict the evolution of the Gulf Stream after it leaves the coast at Cape Hatteras and flows northeastward into the North Atlantic (Robinson et al. 1989a,b; Willems et al. 1994; Lai et al. 1994). In this region the Gulf Stream is characterized by a meandering jet. The amplitude of the meanders increases downstream, and this often leads to the formation of Gulf Stream eddies, or so-called warm and cold core rings. It is the prediction of these meanders and eddies that is of primary interest because of their impact on the local heat and momentum budgets in the North Atlantic, as well as their effect on the local biological and acoustic properties of the water column.

In light of recent advances in the understanding of the stability of dynamical flows, we will examine some of the factors that are likely to govern the growth of initial errors and uncertainties in ocean flows. Errors in the surface forcing and boundary conditions will also have a considerable influence on the predictability of the ocean, but the effects of these errors will not be considered here. The primary focus of this work will be the Gulf Stream, but our results are applicable to other boundary currents and oceanic jets. The results and ideas presented here have been used to develop an ensemble prediction technique for the Gulf Stream, which is described in Moore (1999, hereafter referred to as Part II).

In section 2 we will briefly review some important ideas relating to the stability of stationary and time evolving flows. Here we will introduce the idea of optimal perturbations, which are the fastest growing perturbations that can exist in a dynamical system before the effects of nonlinearity become important. In section 3 we will describe some basic properties of optimal perturbations as they relate to the Gulf Stream, and in section 4 we will examine the stability of different Gulf Stream configurations in the light of optimal perturbation growth. The relationship between optimal perturbations and other possible measures of the stability of the system is examined in section 5. A discussion of our results and findings is given in section 6.

2. Linear stability theory applied to the Gulf Stream

We will briefly review some current ideas regarding the stability of dynamical systems and how they can be applied to the Gulf Stream.

The state of the ocean at any point in space and time can be described by the state variables temperature, salinity, velocity, and so forth. We will denote by Φ a state vector whose elements are the state variables of the ocean at all points in space. Further, we will assume that Φ evolves in space and time according to the nonlinear equation

$$\frac{\partial \Phi}{\partial t} = L(\Phi), \tag{1}$$

where $L(\Phi)$ is a nonlinear operator.

We are interested in the stability of the flow fields described by (1); in particular, how small perturbations ϕ to Φ will evolve. During their early stages of development $\phi^2 \ll \phi$, and the perturbations will be described by linear dynamics, given by the first-order Taylor expansion of (1), namely:

$$\frac{\partial \phi}{\partial t} = \left(\frac{\partial L}{\partial \Phi}\right)\phi. \tag{2}$$

Equation (2) is the so-called tangent linear equation of the system, and by virtue of its linearity, a perturbation $\phi(t_2)$ at some time t_2 is related to the perturbation $\phi(t_1)$ at some earlier time t_1 according to

$$\begin{aligned}\phi(t_2) &= \exp\left(\int_{t_1}^{t_2} (\partial L/\partial \Phi)\, dt\right)\phi(t_1)\\ &= R(t_1, t_2)\phi(t_1),\end{aligned} \tag{3}$$

where $R(t_1, t_2)$ is the linear propagator of the tangent linear Eq. (2). From (3) it is clear that $R(t_1, t_2)$ depends on the evolution of the basic state Φ about which (2) is linearized.

a. The autonomous case

If Φ is stationary or if the linearization in (2) is performed about an instantaneous realization of Φ, then (2) describes an autonomous system and $R(t_1, t_2) = e^{(\partial L/\partial \Phi)\tau}$ where $\tau = t_2 - t_1$. In this case, the eigenvectors of $(\partial L/\partial \Phi)$ are the normal modes of the system and take the form of exponentially growing or decaying perturbations. If (2) is normal, then $R^\dagger(t_1, t_2)R(t_1, t_2) = R(t_1, t_2)R^\dagger(t_1, t_2)$ where $R^\dagger(t_1, t_2)$ is the adjoint of $R(t_1, t_2)$, and the normal modes are orthogonal to each other. In

this case, the growth rate of perturbations is bounded by the fastest growing eigenvector of $(\partial L/\partial\Phi)$, the fastest growing normal mode.

For most geophysical systems of interest, (2) is nonnormal, so $R^\dagger(t_1, t_2)R(t_1, t_2) \neq R(t_1, t_2)R^\dagger(t_1, t_2)$ and the normal modes are nonorthogonal. In this case, perturbation growth over some time interval τ measured in terms of the growth of a norm $\|\phi\|_X$ is determined by the eigenvectors of $R^\dagger(t_1, t_2)XR(t_1, t_2)$, where X is a weight function. When $X = 1$, $\|\phi\|_X$ is the L2 norm of ϕ. The eigenvectors of $R^\dagger(t_1, t_2)XR(t_1, t_2)$ are the singular vectors, or so-called optimal perturbations, of $R(t_1, t_2)$. Optimal perturbations are characterized by rapid transient growth over the interval τ and during this time they can attain large amplitude. This is in contrast to the normal modes that are characterized by continuous exponential growth. If the exponential growth rate of a normal mode is modest, its amplitude will not increase much over a short interval τ. In the absence of unstable normal modes, rapid optimal perturbation growth can still occur.

b. The nonautonomous case

When predicting the evolution of a flow such as the Gulf Stream, we are interested in whether ϕ can grow on a time evolving basic state Φ. In this case, (2) represents a continuous linearization about the time evolving solution $\Phi(t)$ of (1), and as such describes a nonautonomous system. In this situation, $R(t_1, t_2) = \exp\{\int_{t_1}^{t_2} (\partial L/\partial\Phi)\, dt\}$ and depends upon the time history of $\Phi(t)$. The stability of the system described by $R(t_1, t_2)$ cannot therefore be completely described by the eigenvectors of $(\partial L/\partial\Phi)$ since $(\partial L/\partial\Phi)$ varies in time, so the traditional notion of normal modes developed for autonomous systems does not carry over to systems that are nonautonomous [see Farrell and Ioannou (1996a,b) for a detailed discussion of this point].

Traditionally, the stability of nonautonomous systems is described by the first Lyapunov exponent ξ, given by

$$\xi = \lim_{t\to\infty} \sup \frac{\|\ln(R(0, t))\|}{t}. \tag{4}$$

For complex dynamical systems, it may not be pratically possible to reach the limit in (4) until after a very long time has elapsed, so determination of the Lyapunov exponents may not be tractable for such systems. However, since forecasters are typically interested in finite time intervals $t_1 \to t_2$, the eigenvectors of $R(t_1, t_2)$ are often considered instead of the Lyapunov exponents. By analogy with the autonomous case, the eigenvectors of $R(t_1, t_2)$ are sometimes referred to as finite-time normal modes, and they describe the stability of a local portion of the system trajectory $\Phi(t_1) \to \Phi(t_2)$ in phase space.

Unlike the notion of normal modes, the optimal perturbations retain their meaning and relevence in nonautonomous systems, and are the eigenvectors of $R^\dagger(t_1, t_2)XR(t_1, t_2)$ where $R(t_1, t_2)$ is time dependent. As in the autonomous case, the optimal perturbations of nonautonomous systems are characterized by rapid transient growth, even when there are no unstable finite-time normal modes or Lyapunov exponents with $\xi > 0$ (Farrell and Ioannou 1996a,b).

The ideas summarized here provide an illuminating framework for understanding the early stages of linear development of errors and uncertainties in forecast models. At some stage nonlinear effects become important, at which time linear assumptions break down. A large body of literature based on numerical simulations and complex closure theories for turbulent flows exists that attempts to unravel the nonlinear phase of error growth (see Holloway and West 1984). However, as yet no general theory for the nonlinear phase of error growth exists, although extensions of the linear ideas summarized here are beginning to take shape based on the observation that the nonlinear backscatter of growing perturbations can act as a source of stochastic noise forcing generating new perturbations whose development is initially governed by linear dynamics, and so on (see Farrell and Ionnou 1993a, 1996b). A direct numerical simulation approach to the problem of the predictability of the Gulf Stream based on the ideas of linear stability theory and stochastic–dynamic prediction is presented in Part II.

c. The model Gulf Stream

As shown by Farrell and Ioannou (1996a,b), optimal perturbation theory extends naturally from autonomous systems to nonautonomous systems, and for this reason is the appropriate framework for studying the predictability of time evolving flow fields. In this vein, we have applied optimal perturbation theory to a model of the Gulf Stream. The model used was a quasigeostrophic ocean model originally developed by Haidvogel et al. (1980) and Miller et al. (1981). The nondimensional quasigeostrophic equations of motion for streamfunction ψ and vorticity ζ are given by

$$\frac{\partial\zeta}{\partial t} + \alpha J(\psi, \zeta) + \beta\frac{\partial\psi}{\partial x} + F(\zeta) = 0 \tag{5}$$

$$\zeta = \nabla^2\psi + \frac{\partial}{\partial z}\left(\frac{1}{S}\frac{\partial\psi}{\partial z}\right), \tag{6}$$

where $\alpha = V_0 t_0/D$, $\beta = \beta_0 D t_0$, and $J(\cdots, \cdots)$ is the Jacobian operator. The horizontal velocity, horizontal distance, time, height, and Brunt–Väisälä frequency N^2 are scaled by V_0, D, t_0, h, and N_0^2, respectively. In this case, $S = (L_D/D)^2$, where $L_D = Nh/f_0$ is the Rossby radius of deformation. The Coriolis parameter $f_0 = 2\Omega \sin\theta_0$, where Ω is the angular velocity of the earth due to rotation and θ_0 is the central latitude of the model domain. Here $F(\zeta)$ is a dissipation term in the form of an eighth-order Shapiro filter operating on vorticity (Shapiro 1970).

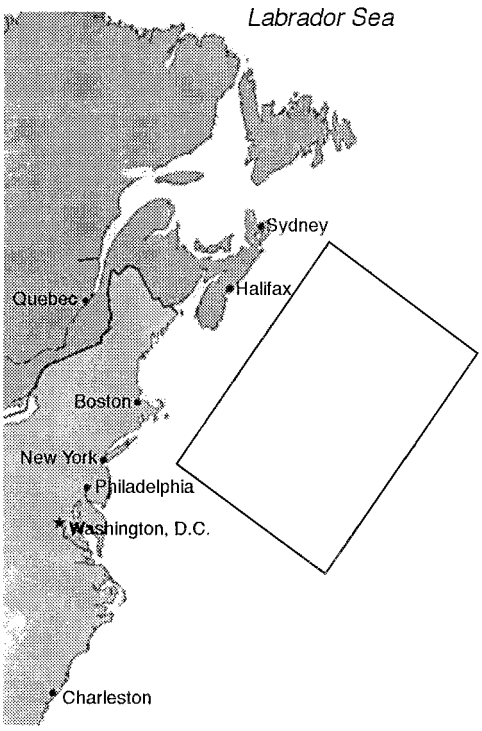

FIG. 1. A schematic showing the geographical location and orientation of the ocean model domain.

Equations (5) and (6) were solved in an open ocean domain using the open boundary conditions of Charney et al. (1950). This amounts to specifying ψ on all open boundaries and specifying ζ at points where the flow described by ψ is directed toward the interior of the domain. At the top and bottom, the following boundary conditions are applied:

$$\frac{\partial^2\psi}{\partial t\partial z} + \alpha J(\psi, \partial\psi/\partial z) = -Sw \quad \text{at } z = 0 \quad \text{and} \quad z = -H, \tag{7}$$

where w is the vertical velocity associated with surface forcing and flow over bathymetry. We will consider an unforced system with a uniform depth H (i.e., a flat bottom), in which case $w = 0$ at both $z = 0$ and $z = -H$. Complete details of the discretization of (5)–(7) and the solution techniques can be found in Haidvogel et al. (1980) and Miller et al. (1981), and will not be discussed here.

The derivation of the tangent linear form of (5)–(7) and their adjoint is straightforward and is described in Moore (1991) and Moore and Farrell (1993). The solution techniques of the tangent linear model and its adjoint are also described by these authors and will not be described here.

The model domain was configured as shown in Fig. 1, centered at 38.3°N, 62.8°W in the Gulf Stream meander and ring region, with a horizontal resolution of 15 km and four levels in the vertical centered at depths 150 m, 450 m, 800 m, and 2750 m. The model domain is 1350 km in length and 720 km wide. The nondimensional parameters in (5) and (6) relevant to the Gulf Stream are $V_0 = 0.4$ m s^{-1}, $D = 40$ km, $t_0 = 4$ days, $h = 700$ m and $N_0^2 = 1.9 \times 10^{-5}$ s^{-2}, and $L_D \sim 73$ km at the ocean surface.

3. Optimal perturbations of the Gulf Stream: Some basic properties

Gulf Stream flows were initialized in the model using the thin jet feature models described by Robinson et al. (1988). The position of the Gulf Stream north edge (the frontal region separating the cold waters of the North Atlantic from the warmer waters of the Sargasso Sea) and Gulf Stream rings can be determined from satellite data. The digitized position of the north edge can then be used in conjunction with feature models to construct model initial conditions. The north wall position data used here were processed by Chin and Mariano (1997) using contour analysis techniques described by Mariano (1990). The velocity profile for the Gulf Stream feature model jet as a function of cross-stream position l and depth z is given by

$$V(l, z) = \begin{cases} e^{-l^2/g_{n,s}^2}[v_d - (v_0 - v_d)z/d] & \text{for } -d \le z \le 0 \\ e^{-l^2/g_{n,s}^2}[v_H - (v_d - v_H) \\ \qquad \times (z - H)/(H - d)] & \text{for } z < -d, \end{cases} \tag{8}$$

where v_0, v_d, and v_H are the velocities at $z = 0$, $z = -d$, and $z = -H = -4500$ m (the bottom of the ocean), respectively, and $g_{n,s}$ is the e-folding width of the stream to the north (n) and south (s) of the stream axis. The initial cross-stream and vertical velocity profiles are independent of the alongstream direction. The standard configuration we will use in the experiments below is $v_0 = 2$ m s^{-1}, $v_d = 0.5$ m s^{-1}, $v_H = 0.05$ m s^{-1}, $d = 1000$ m, and $g_n = g_s = 40$ km, which yields a jet structure typical of that observed in the real Gulf Stream (Watts and Johns 1982). The positions of Gulf Stream rings were not included in the feature model initial conditions of the experiments described here because of poorer quality data on their position and to keep this initial study focused on the influence of meander growth on the growth of errors and uncertainties.

In this section we will examine some basic properties of the optimal perturbations of a flow field that is typical of those examined in section 4. The optimal perturbations for different time varying basic-state flows were computed iteratively using the tangent linear ocean model, the adjoint of the tangent linear model, and the ARPACK Lanczos algorithm SSAUPD described by Sorensen (1992). The basic-state flows were generated by initializing the nonlinear quasigeostrophic model described by (5)–(7) with a feature model initial condition computed from (8) using the observed position of the Gulf Stream north wall. The nonlinear model was run

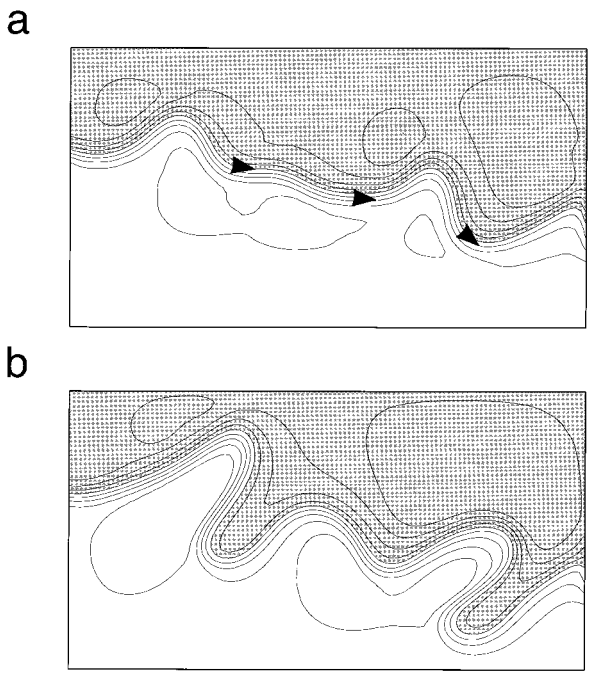

FIG. 2. Maps of surface streamfunction ψ for the Gulf Stream basic state initialized on 1 Jan 1990. Each panel shows the configuration of the Gulf Stream 8 days apart. The arrows in (a) show the direction of flow, and in each case shading indicates where $\psi < 0$. The contour interval is one nondimensional unit.

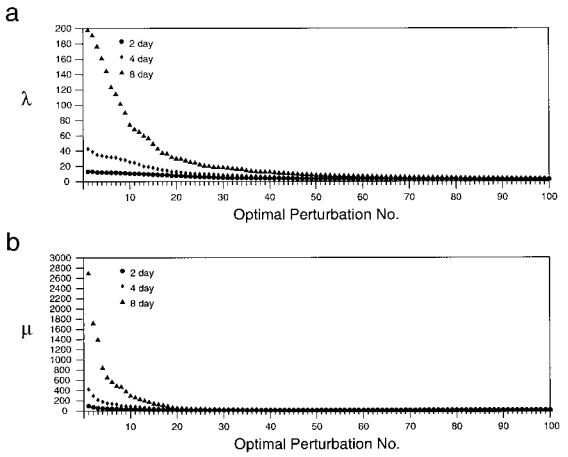

FIG. 3. The spectrum of growth factors of the first 100 optimal perturbations for the time evolving Gulf Stream flow initialized on 1 Jan 1990 (cf. Fig. 2) for three different optimal growth times τ. (a) The growth factors λ of the total perturbation energy for the energy optimal spectrum and (b) the growth factors μ of perturbation potential enstrophy for the enstrophy optimal spectrum.

forward in time over the interval $t = 0 \rightarrow 8$ days to allow a dynamically interesting and realistic flow field to develop in the model. The model was then run for a further period $t = 8 \rightarrow 16$ days and the basic-state state vector $\Phi \equiv \zeta$ saved.

For the quasigeostrophic model used here, there are two natural norms for measuring the growth of perturbations in the system. These are the perturbation energy norm $E = -1/2\langle \delta\zeta, \delta\psi \rangle$ and the perturbation enstrophy norm $Q = \langle \delta\zeta, \delta\zeta \rangle$ where $\langle \cdots, \cdots \rangle$ defines the L2 norm. We will consider the optimal perturbations of both the E and Q norms and refer to these perturbations as ''energy optimals'' and ''enstrophy optimals,'' respectively.

The basic state used in all of the calculations of this section was derived using the observed position of the Gulf Stream north wall on 1 January 1990. Maps of the basic-state surface streamfunction ψ, 8 days apart, are shown in Fig. 2 and reveal how meanders propagate downstream and steepen. There is nothing remarkable about the resulting flow configuration in the model during this time, and it is typical of the kinds of flows observed in the real ocean. We will postpone any further discussion of the basic-state flow until section 4 when we consider the energetics of the system. For now we will confine our attention to some general properties of the optimal perturbation spectra using this basic state.

Figure 3a shows the perturbation energy growth factors, hereafter identified as λ, of the first 100 members of the energy optimal spectrum for a nonautonomous tangent linear system using the basic state shown in Fig. 2. Three different time intervals $\tau = t_2 - t_1$ are considered, namely 2, 4, and 8 days. Hereafter we refer to τ as the ''optimal growth time'' since this is the interval during which λ grows most rapidly. Figure 3a shows that over a 2–4 day optimal growth period E for the fastest growing members of the energy optimal spectra typically increases by an order of magnitude. Over a longer period ($\tau = 8$ days) typical of the duration of a Gulf Stream forecast, E can grow by two orders of magnitude (≡an order of magnitude increase in the amplitude of ϕ). Figure 3a also shows that, as τ increases, the spectrum becomes dominated by a few rapidly growing members, and when $\tau = 8$ days, there are only seven energy optimals with growth factors $\lambda \geq 100$ (i.e., that increase in amplitude by a factor of 10 or more). The total number of members of the energy optimal spectrum is equal to the total number of grid points in the model, which is $91 \times 49 \times 4$ levels = 17 836. Therefore, for $\tau = 8$ days only a very small fraction of the energy optimal spectra undergo significant growth.

Figure 3b shows the Q growth factor, hereafter denoted μ, of the first 100 members of the enstrophy optimal spectrum. In general $\mu \sim 10\lambda$ for a given τ, implying an efficient straining of the small-scale vorticity field by the large-scale flow. The shape of the spectrum varies with τ in a similar way to that of the energy optimals of Fig. 3a.

The spectra of energy and enstrophy optimals for an autonomous tangent linear system (not shown) are very similar to those in Fig. 3. In this case snapshots of the time evolving basic state at $t = t_1$ are used as the basic state of the tangent linear model.

We will now examine the perturbation energy growth

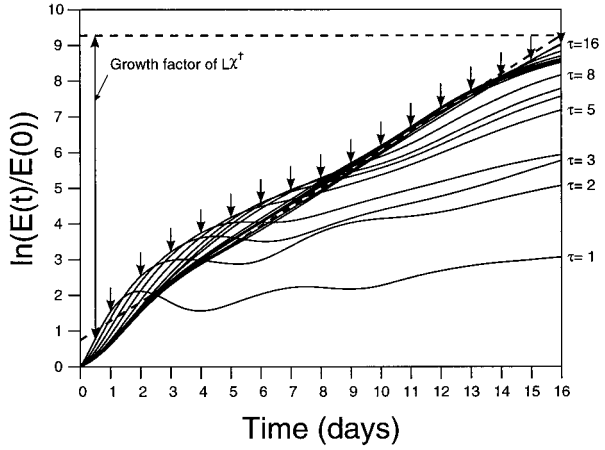

FIG. 4. Times series of $\ln[E(t)/E(0)]$ over a 16-day period for energy optimals of the time evolving basic-state flow initialized on 1 Jan 1990 (cf. Fig. 2), where $E(t)$ is the domain integrated perturbation energy of the system as a function of time. Times series are shown for energy optimals that have optimal growth times τ ranging from 1 to 16 days. The arrows indicate $\ln(\lambda) = \ln[E(\tau)/E(0)]$ for each energy optimal at the end of its optimal growth time τ. The growth factor of $\mathcal{L}\chi^\dagger$ discussed in section 5 is also indicated.

characteristics and spatial structure of the optimal perturbations for the basic state described above. Figure 4 shows time series of $\ln[E(t)/E(0)]$ for the fastest growing energy optimals that result for different values of τ ranging from 1 to 16 days. For each energy optimal, Fig. 4 shows the evolution of $\ln[E(t)/E(0)]$ over a 16-day period on the time evolving basic state. The vertically orientated arrows above each curve indicate the values of $\ln[E(\tau)/E(0)]$ at the optimal growth time τ for each energy optimal. Each perturbation initially has unit perturbation energy so values of $\ln[E(\tau)/E(0)]$ at τ are equivalent to $\ln(\lambda)$. Figure 4 shows a number of interesting features. First, it is apparent that each energy optimal continues to grow rapidly for some time after its optimal growth time and growth factor λ have been reached. This is particularly true when $\tau \geq 5$ days. Second, all of the energy optimals eventually continue to grow after several days have elapsed, even after, in some cases, a temporary period of energy decrease. These characteristics of the optimal perturbations will be discussed further in section 5 in connection with the relationship between optimal perturbations and finite-time normal modes. Third, we note in Fig. 4 that the initial growth *rate* of perturbations during their early stages of growth decreases with increasing τ. For example, the energy optimal for $\tau = 1$ day initially grows $\sim$3 times faster during the first day than the energy optimal for $\tau = 16$ days. This aspect of optimal perturbation growth can be understood in terms of their structure and energetics as discussed in section 4b.

Figure 5 shows the initial configuration of perturbation streamlines $\delta\psi$ for energy optimals for a range of τ between 1 and 16 days. For $\tau \leq 6$ days, a general feature of the energy optimals is that their horizontal scale increases with τ. For $\tau = 1$ day, perturbations have the shortest wavelengths and are initially configured as a series of ''arrowheads'' pointing upstream. As τ increases, the wavelength of the initial arrowhead structures and their length increases resulting in a more pronounced upstream tilt of $\delta\psi$. This aspect of optimal perturbation behavior can be understood from an analysis of their energetics, presented in sections 4b and 4d.

Figure 5 shows that there is an abrupt change in the initial structure of $\delta\psi$ at $\tau = 9$ days, which remains largely unchanged for $\tau \geq 9$ days. A change in the growth characteristics of E is also evident in Fig. 4 for $\tau \geq 9$ days when all of the energy optimals grow at a very similar rate, and after 3 days of development this is close to a constant exponential growth rate. The change in structure of the energy optimals and their growth characteristics at $\tau = 9$ days is related to the rapid steepening of the meanders in the eastern portion of the model around this time. There will be more discussion of the effects of a time evolving basic state on perturbation growth in section 4.

The growth characteristics of the enstrophy optimals with different optimal growth times $\tau = 1 \rightarrow 16$ days are shown in Fig. 6, which shows the growth of $\ln[Q(t)/Q(0)]$ over a 16-day period for each case. The natural log of the perturbation enstrophy growth factor μ after the optimal growth time has elapsed is indicated by the arrows. In each case, the enstrophy optimals continue to grow rapidly after their optimal growth time has been reached. After 6 days or so they all grow with a similar, almost constant, exponential growth rate. The initial configuration of the perturbation vorticity $\delta\zeta$ for enstrophy optimals with a range of optimal growth times is shown in Fig. 7.[1] An important feature to note in Fig. 7 is that for τ greater than about 5 days, the structures of $\delta\zeta$ for the enstrophy optimals have many features in common with the structure of $\delta\psi$ for the energy optimals shown in Fig. 5. We will return to this important feature of the optimal perturbations of the E and Q norms in section 5.

The streamfunction of an optimal perturbation undergoes a change in scale as it grows. For energy optimals the scale of $\delta\psi$ increases while for enstrophy optimals the scale of $\delta\psi$ decreases. Interestingly, even though they are linear, the change in scale of the optimal perturbations is very reminiscent of the energy and enstrophy cascades that occur in a nonlinear system. It may be that the dynamics of the optimal perturbations represents the linear stages of these cascades before nonlinearity becomes important, but this is merely speculation.

[1] We show $\delta\zeta$ rather than $\delta\psi$ because Q is given by the L2 norm of $\delta\zeta$. Examples of $\delta\psi$ for enstrophy optimals may be found in Part II.

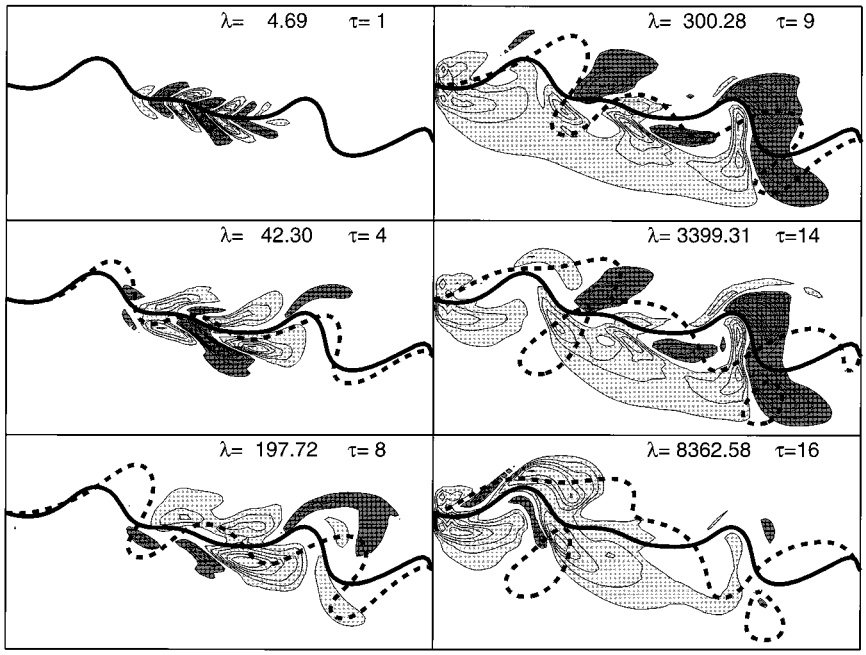

FIG. 5. Maps of surface perturbation streamfunction $\delta\psi$ for the fastest growing energy optimals of the time evolving Gulf Stream flow initialized on 1 Jan 1990 (cf. Fig. 2). The optimal structures are shown for different values of optimal growth time τ ranging from 1 to 16 days. The perturbation energy growth factor λ is indicated in each case. Light shading indicates where $\delta\psi > 0$ and dark shading where $\delta\psi < 0$. The heavy solid and dashed lines indicate the position of the Gulf Stream axis at initial time and at the optimal growth time, respectively. Since the optimal perturbations are the eigenvectors of a linear operator, the contour interval is arbitrary.

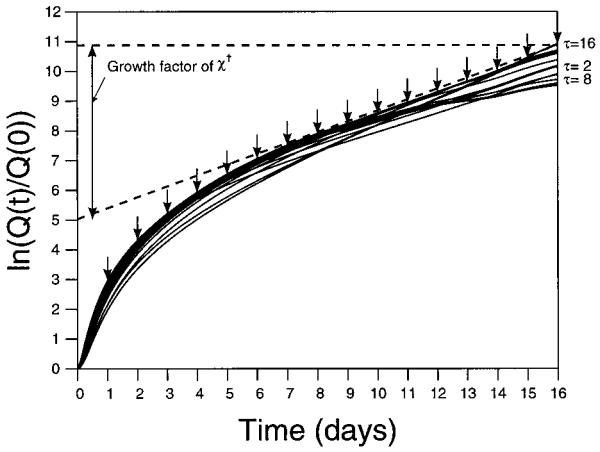

FIG. 6. Times series of $\ln[Q(t)/Q(0)]$ over a 16-day period for enstrophy optimals of the time evolving basic-state flow initialized on 1 Jan 1990 (cf. Fig. 2), where $Q(t)$ is the domain integrated perturbation potential enstrophy of the system as a function of time. Times series are shown for enstrophy optimals that have optimal growth times τ ranging from 1 to 16 days. The arrows indicate $\ln(\mu) = \ln[Q(\tau)/Q(0)]$ for each enstrophy optimal at the end of its optimal growth time. The growth factor of $\chi^{\dagger}$ discussed in section 5 is also indicated.

4. The stability of different flow configurations

Of obvious interest is how the structure, growth rate, and location of preferred growth of optimal perturbations varies with the configuration of the Gulf Stream flow since this reveals how error growth may be influenced by the time evolving flow in a model forecast. As an illustration of the variety of flow configurations that we might expect to observe, Fig. 8 shows the surface streamfunction ψ from the quasigeostrophic model using the feature model initial conditions given (8) and the observed position of the Gulf Stream north wall on selected days during 1990. A variety of interesting and sometimes complex Gulf Stream flows, reminiscent of the kinds of flow fields we might expect to observe in nature, are shown in Fig. 8.

In an operational environment, forecasts of the Gulf Stream can be made in much the same way as weather forecasts by initializing a forecast model with a best estimate of the current state of the system. This best estimate is typically based on recent observations and the most recent model forecast. In this vein, we can therefore think of the Gulf Stream flows in Fig. 8 as typical examples of possible estimates of the initial conditions for forecasts of the Gulf Stream that might result from some operational analysis and data assimilation procedure. With this in mind, it is of considerable interest to examine the potential for error growth in the

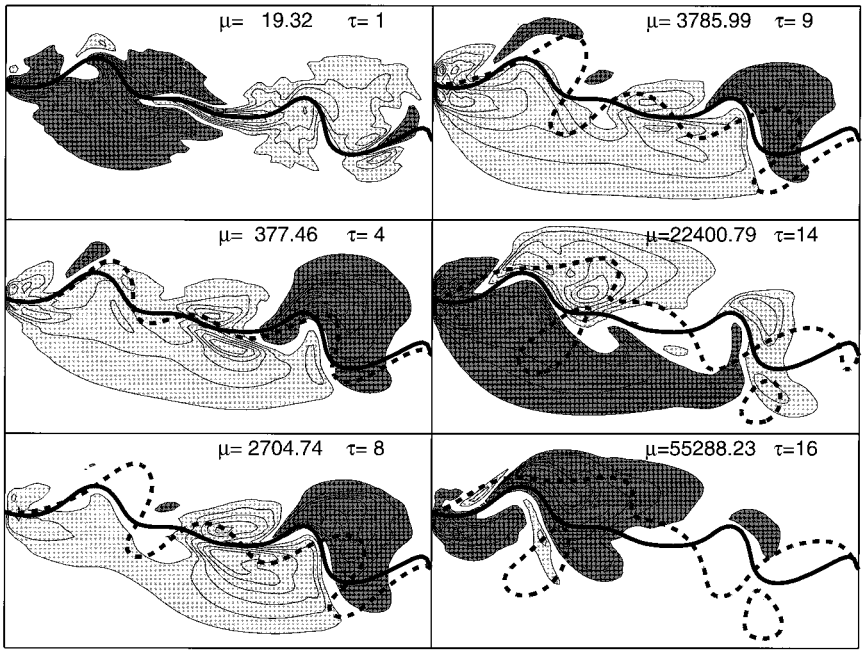

FIG. 7. Maps of surface perturbation vorticity $\delta\zeta$ for the fastest growing enstrophy optimals of the time evolving Gulf Stream flow initialized on 1 Jan 1990 (cf. Fig. 2). The optimal structures are shown for different values of optimal growth time τ ranging from 1 to 16 days. The perturbation energy growth factor μ is indicated in each case. Light shading indicates where $\delta\zeta > 0$ and dark shading where $\delta\zeta < 0$. The heavy solid and dashed lines indicate the position of the Gulf Stream axis at initial time and at the optimal growth time, respectively. The contour interval is arbitrary.

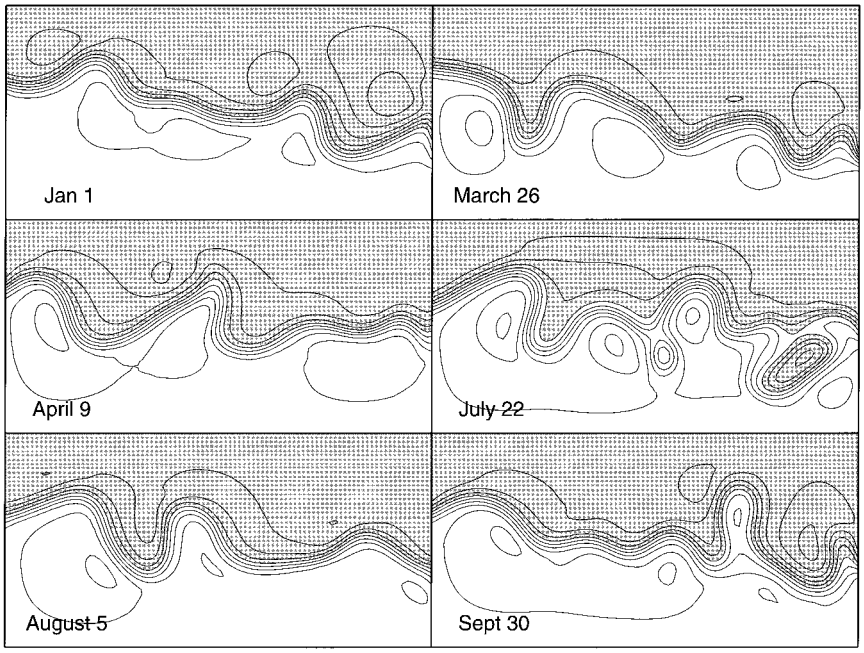

FIG. 8. Snapshots of the surface streamfunction ψ for a selection of different basic-state simulations of the Gulf Stream 8 days after the feature model initialization on the dates indicated during 1990. Shading indicates where $\psi < 0$. The contour interval is one nondimensional unit.

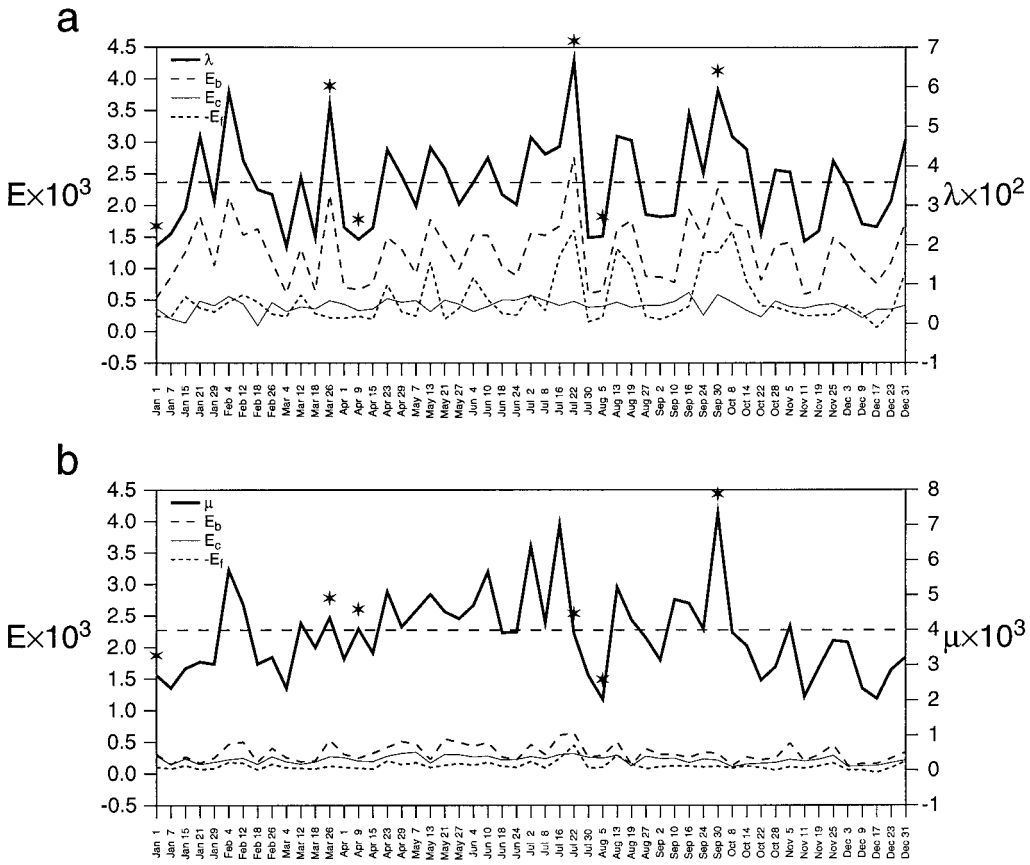

FIG. 9. The growth factors of the fastest growing members of the optimal perturbation spectra for time evolving basic-state flows initialized on the dates indicated. In each case the optimal growth time $\tau = 8$ days. (a) The perturbation energy growth factors λ for the fastest growing energy optimal. (b) The perturbation enstrophy growth factors μ for the fastest growing enstrophy optimal. The horizontal dashed lines indicate the annual mean values of λ and μ. Also shown are $\mathcal{E}_b$, $\mathcal{E}_c$, and $\mathcal{E}_f$ for each optimal (see section 4b for definitions) in nondimensional units. The asterisks indicate the cases shown in Figs. 11 and 14, and the horizontal dashed line shows the annual average values of λ and μ.

flow fields that result from the different initial conditions of Fig. 8 since the location and rate of error growth in the system will provide information about the predictability of different flow features and dynamical events. These ideas have been applied directly to the problem of ensemble prediction of the Gulf Stream in Part II.

Motivated by the above arguments, the flow field configurations in Fig. 8, along with 47 other cases also originally derived from feature models of the observed conditions in 1990, were used as initial states for the quasigeostrophic model. Starting from each initial condition, the model was run forward in time for 8 days to generate a time evolving basic state as described in section 3. In all a total of 53 cases were considered and generated from feature models using the observed position of the Gulf Stream every week during 1990. We will think of the resulting basic-state flow fields as one year of Gulf Stream forecasts. The optimal perturbation spectra of each time evolving basic state were computed for both the E and Q norms using an 8-day optimal growth time τ. Figure 9a shows the perturbation energy growth factors λ of the fastest growing energy optimal of the 53 weekly ''forecasts.'' The mean value of λ is 358 although there is much variability throughout the year about the mean. The variation in the growth factor μ of the fastest growing enstrophy optimals for each forecast is shown in Fig. 9b. As noted earlier, Q of the enstrophy optimals typically grows an order of magnitude more than E of the energy optimals. However, the variations of λ and μ about their annual mean values are generally in phase, being above and below average at roughly the same times.

a. Validity of the tangent linear approximation

At this point, it is pertinent to discuss the validity of the tangent linear equation (2) as it relates to the quasigeostrophic model described by (5), (6), and (7). This was assessed in the following way: (i) Each of the basic states in 1990 were perturbed by their fastest growing

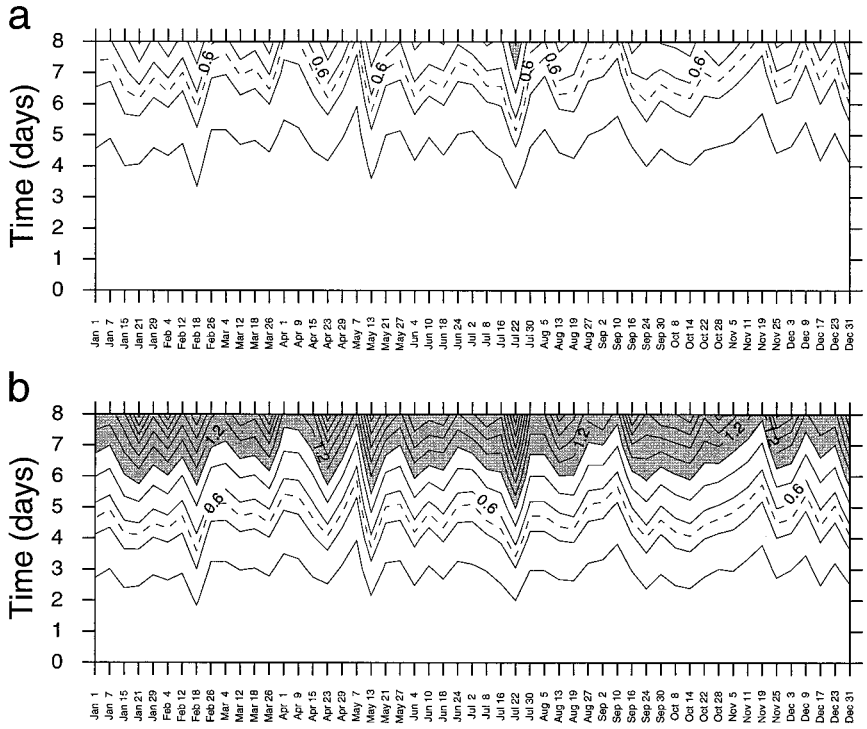

FIG. 10. Contours of the normalized rms error R_ψ in the tangent linear approximation as a function of time for two different optimal perturbation amplitudes A, (a) $A = 0.1$ and (b) $A = 0.2$. Shading indicates where R_ψ exceeds the equivalent of a 100% error in the tangent linear approximation, and the dashed contour indicates where $R_\psi = 0.5 \equiv 50\%$ error. The contour interval is 0.2.

energy optimals with amplitude A and the nonlinear model described by (5)–(7) integrated forward in time for 8 days. The difference between this and an unperturbed integration of the nonlinear model (i.e., with $A = 0$) was then computed. The differences in ψ between these two model integrations will be denoted $\Delta\psi$. (ii) The fastest growing optimal perturbation of the energy norm of each basic state from 1990 was integrated forward in time for 8 days using the tangent linear quasigeostrophic model derived from (5)–(7). The perturbation streamfunction from the tangent linear model is denoted $\delta\psi$. (iii) The rms difference, R_ψ, between $\Delta\psi$ of (i) and $\delta\psi$ of (ii) was computed as an average over the entire model domain each day according to

$$R_\psi = \left[\sum_i \sum_j \sum_k (\Delta\psi_{ijk} - \delta\psi_{ijk})^2\right]^{1/2} \Bigg/ \left[\sum_i \sum_j \sum_k \psi_{ijk}^2\right]^{1/2}, \tag{9}$$

where the subscripts i and j reference model grid points in the horizontal, subscript k references grid points in the vertical, and the denominator in (9) represents the domain-averaged rms value of streamfunction ψ from the unperturbed nonlinear model solution described in (i). Figure 10 shows contours of R_ψ as a function of time for all basic states considered in 1990. Two different values of perturbation amplitude were considered corresponding to $A = 0.1$ and 0.2. Relative to the domain-integrated rms initial streamfunction of each unperturbed basic state, these two cases correspond to initial errors in ψ of approximately 5% and 10%, respectively. The dashed contour in each panel of Fig. 10 indicates where R_ψ is equivalent to a 50% error measured relative to the unperturbed basic state ψ. A value of $R_\psi \sim 50\%$ could justifiably be chosen as the point where the tangent linear approximation seriously breaks down. Values of R_ψ in excess of 100% are shaded in Fig. 10. For $A \sim 5\%$, the tangent linear approximation is valid for ~ 7 days, although there is much variation in R_ψ due to the differing growth rates of the fastest growing optimal perturbations. For rapidly growing perturbations, R_ψ reaches 50% in around 5 days. As A increases to $\sim 10\%$, levels of R_ψ reach 50% in around 4–5 days.

Since the optimal perturbations are the fastest growing disturbances that can exist in the system, the 2–7 day timescale indicated in Fig. 10 can be thought of as a lower bound on the validity of the tangent linear approximation. Errors of 5%–10% would not be uncommon in observations of the Gulf Stream flow and in initial conditions resulting from objective analyses and data assimilation, so we conclude that for the quasi-

geostrophic model used here the tangent linear approximation will be valid for at least ~4–7 days.

b. Analyses of energy optimals

Figure 11 shows the configuration of $\delta\psi$ before and after optimal growth for the fastest growing energy optimals of the forecasts arising from each of the model initial conditions shown in Fig. 8. Clearly there is much variation in the initial structure and preferred region of growth of the fastest growing energy optimals. The asterisks in Fig. 9a indicate the optimal perturbations shown in Fig. 11.

To understand the structure and preferred region of growth of the energy optimals in Fig. 11, it is necessary to consider their energetics. The domain integrated change in perturbation energy of a perturbation is given by

$$\int_0^{L_x}\int_0^{L_y}\int_{-H}^{0} E(t_2) - E(t_1)\, dx\, dy\, dz = \mathcal{E}_b + \mathcal{E}_c + \mathcal{E}_f. \tag{10}$$

In (10), $\mathcal{E}_b$ and $\mathcal{E}_c$ represent the perturbation energy release due to barotropic and baroclinic processes, respectively, and $\mathcal{E}_f$ represents the dissipation of perturbation energy by the Shapiro filter $F(\zeta)$. The functional forms of $\mathcal{E}_b$ and $\mathcal{E}_c$ are well known and are given in Moore and Farrell (1993) for the model used here. Figure 9a shows $\mathcal{E}_b$, $\mathcal{E}_c$, and $\mathcal{E}_f$ for the fastest growing energy optimal of each flow configuration, and typically $\mathcal{E}_b \gg \mathcal{E}_c$ in each case. However, as we will demonstrate in section 4d, the partitioning of perturbation energy between $\mathcal{E}_b$ and $\mathcal{E}_c$ is sensitive to the feature model parameters in (8) that control the shearing and straining components of the flow.

While $\mathcal{E}_c \ll \mathcal{E}_b$, energy release by baroclinic processes is by no means negligible. To illustrate, Fig. 12 shows maps of the time integrated, vertically integrated Reynolds eddy stresses and the eddy heat fluxes that contribute to $\mathcal{E}_b$ and $\mathcal{E}_c$ for the case where the basic state ψ is that of Fig. 2. Figure 12 shows that locally, energy release by barotropic and baroclinic processes is comparable, although for $\mathcal{E}_c$, regions in which perturbation energy is liberated from the basic-state flow ($\mathcal{E}_c > 0$) are largely balanced downstream by regions where perturbation energy would be given up to the basic-state flow ($\mathcal{E}_c < 0$).

The localized nature and geographic location of $\mathcal{E}_b$ and $\mathcal{E}_c$ in Fig. 12 can be understood by examining the evolution of the basic-state flow field. The maps of ψ shown in Fig. 2 reveal how meanders propagate downstream and steepen. As this happens, straining regions develop in the flow at the head of and in the lee of the meanders as evidenced by the diverging and converging streamlines in these regions. The dynamics responsible for these changes in the Gulf Stream is discussed in some detail by Spall and Robinson (1990). Some of the changes that occur in ψ in these regions as the flow evolves are quite subtle. However, despite these subtleties, such regions of evolving flows are highly favored for growth by barotropic processes as evidenced by the initial configurations of the $\delta\psi$ shown in Fig. 11, which often show pronounced upstream tilts of phase lines in the horizontal plane. Similar findings are noted by Farrell (1990) for idealized flows. The tendency of streamlines to slope upstream in the horizontal when energy release by barotropic processes is important is discussed by Pedlosky (1987) and in detail by Zeng (1983).

Figure 11 indicates that often times (e.g., 26 March, 22 July, and 30 September), large growth factors λ accompany the formation of deep meanders in the basic-state flow field. At the apex of a meander, the basic-state flow is undergoing a rapid change in direction so this is a region of straining flow. As these regions develop they are often favored for growth by optimal perturbations via barotropic processes. The interaction of eddies with the main Gulf Stream jet can also create favorable conditions for optimal perturbation growth by creating regions of straining flow. An example of such a case is evident in Fig. 11 on 22–29 July.

Clearly, the development of straining regions in the flow will influence error growth in forecast models and affect the predictability of the flow. Figure 3 shows that typically ~10 energy optimals have significant energy growth factors, so other members of the spectrum are also likely to be important for characterizing error growth in the system. Figure 13 shows the initial configuration of $\delta\psi$ for the first six members of the energy optimal spectrum for the time evolving basic state of Fig. 2. In each case the perturbations single out the regions of straining flow in the basic state to achieve rapid growth.

c. Analyses of enstrophy optimals

Figure 14 shows the initial configuration of $\delta\zeta$ for the fastest growing enstrophy optimals on the dates indicated. The initial conditions of the time evolving basic state flows are shown in Fig. 8. A comparison of Fig. 14 with Fig. 11 shows that the enstrophy optimals often share many features in common with the energy optimals, and in some cases $\delta\psi$ and $\delta\zeta$ are very similar. The asterisks in Fig. 9b indicate the optimal perturbations shown in Fig. 14.

Energy analyses of the enstrophy optimals (not shown) reveal that they typically develop and grow in the same geographical regions as the energy optimals. While the growth factor of E of the enstrophy optimals is typically an order of magnitude less than that of E for the energy optimals, the geographical distributions of $\mathcal{E}_b$ and $\mathcal{E}_c$ are similar in each case, indicating that both kinds of optimal perturbations rely for their growth on the development of the same straining features in the basic-state flow. Figure 9b shows that $\mathcal{E}_b \sim \mathcal{E}_c$ for the enstrophy optimals. The enstrophy optimals seek out areas of straining flow where

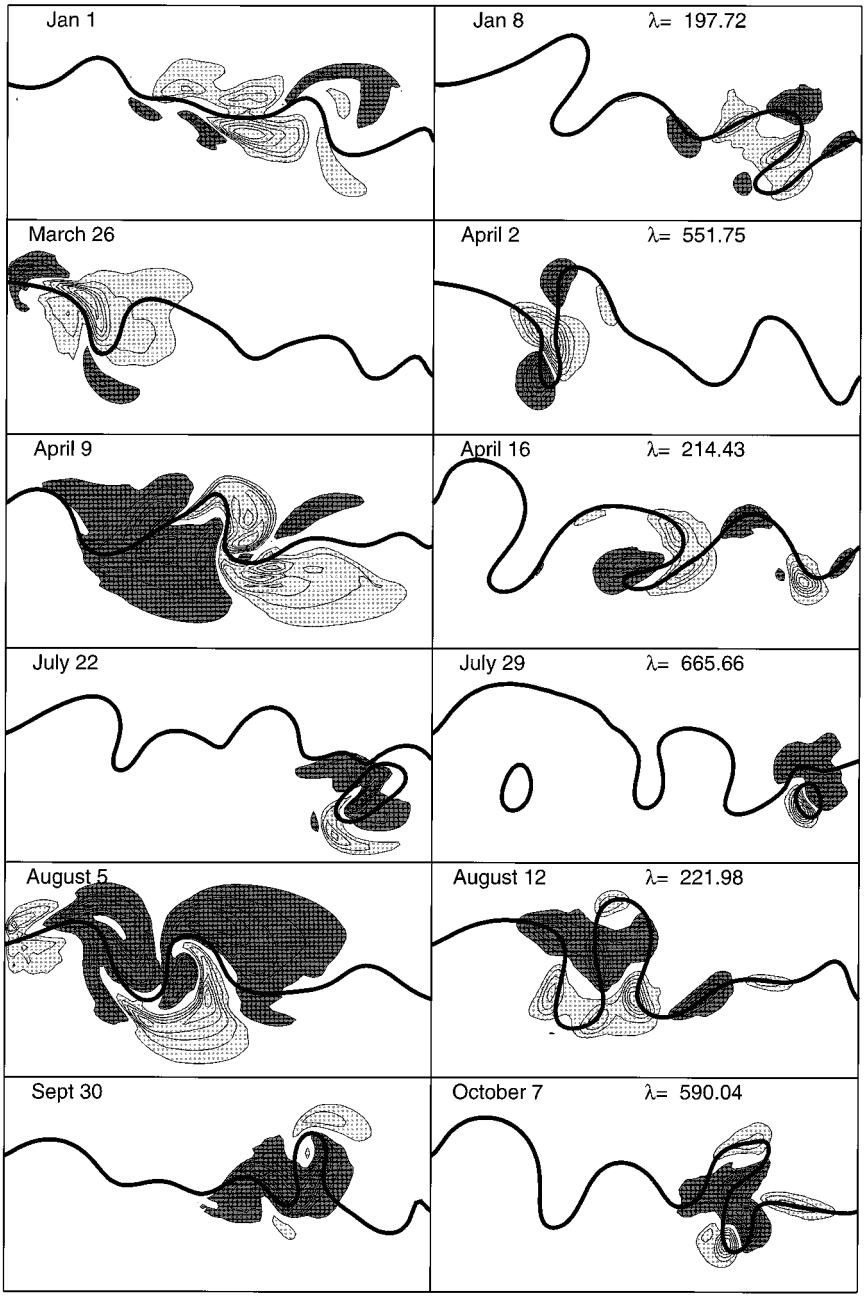

FIG. 11. Maps of surface perturbation streamfunction $\delta\psi$ before (left-hand panels) and after (right-hand panels) optimal growth for the fastest growing energy optimals of the time evolving Gulf Stream flows on the dates indicated. The initial configurations of the Gulf Stream basic state in each case are shown in Fig. 8. The optimal growth time $\tau = 8$ days and the perturbation energy growth factor λ is indicated in each case. Light shading indicates where $\delta\psi > 0$ and dark shading where $\delta\psi < 0$. The heavy solid shows the position of the Gulf Stream axis on the dates indicated. The contour interval is arbitrary.

they can grow by extracting energy from the basic state, and as they grow $\delta\zeta^2$ increases by eddy vorticity flux divergence. Enstrophy optimals behave in the same way as energy optimals in the presence of developing meanders and eddies (see section 4b).

d. The effects of increasing shear

The results of sections 4b and 4c show how natural variations in the straining rate of the basic state can influence optimal perturbation development. The effects

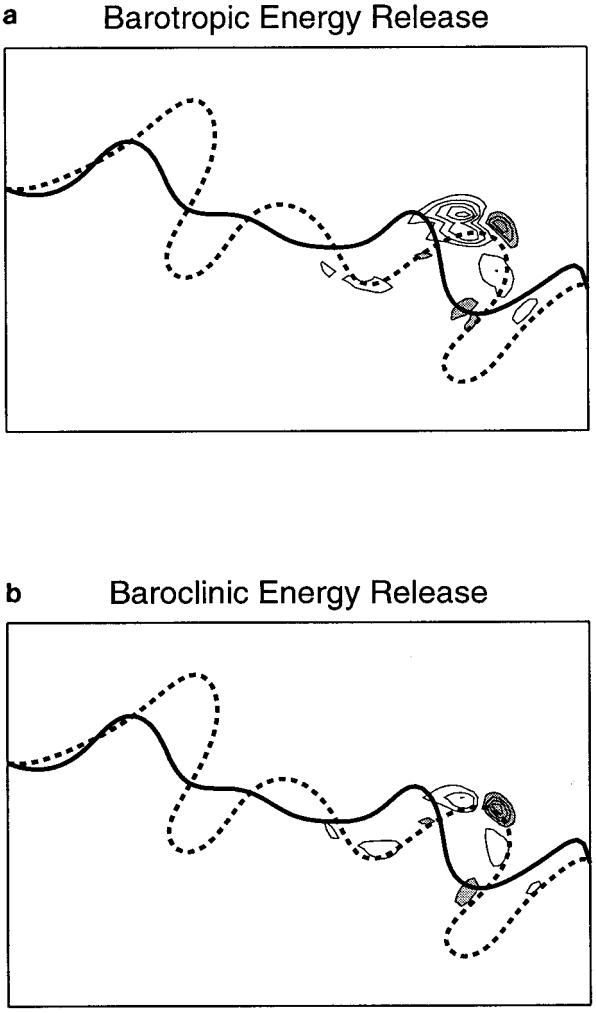

FIG. 12. Contours of the vertically and temporally integrated perturbation energy released over an 8-day period by barotropic and baroclinic processes by the fastest growing optimal perturbation of the time evolving Gulf Stream initialized on 1 Jan 1990. The optimal growth time $\tau = 8$ days. Shading indicates where perturbation energy release is negative and represents regions where the perturbation would give up energy to the basic-state flow. The heavy solid and dashed lines indicate the position of the Gulf Stream axis at initial time and at the optimal growth time, respectively. The contour interval is arbitrary and is the same in both (a) and (b).

of shear in the basic-state flow on the optimal perturbations can be explored by varying the parameters in the feature model (8).

Earlier we examined the dynamics of optimal perturbations for which $\mathcal{E}_b \gg \mathcal{E}_c$. A minor modification of the feature model parameters in (8) can change dramatically the partitioning of basic-state energy release between $\mathcal{E}_b$ and $\mathcal{E}_c$. To illustrate, Fig. 15 shows λ, $\mathcal{E}_b$, $\mathcal{E}_c$, and $\mathcal{E}_f$ for energy optimals that result from nonautonomous basic states generated from the observed Gulf Stream positions in 1990 when the vertical shear is increased by decreasing d in (8) from 1000 to 700 m. In each case $\tau = 8$ days. In general $\mathcal{E}_b \ll \mathcal{E}_c$ in the $d = 700$ m cases, and λ is an order of magnitude larger than the cases shown in Fig. 9a for which $d = 1000$ m.

Figure 16 shows the initial configuration of surface $\delta\psi$ when $d = 700$ m on the same dates as the $\delta\psi$ shown in Fig. 11. It is interesting to compare the structures of these two sets of optimal perturbations. In Fig. 11, $d = 1000$ m and $\mathcal{E}_b$ dominates the perturbation energy budget of the optimal perturbations, while in Fig. 16, $d = 700$ m and $\mathcal{E}_c$ is the dominant energy term. Figures 11 and 16 show, however, that the basic state typically evolves in a similar way for the cases shown. The structure of the energy optimals on the other hand is quite different in the two figures on corresponding dates. When $\mathcal{E}_b$ is dominant the initial perturbation structures generally have a larger scale in the horizontal, while when $\mathcal{E}_c$ is dominant the horizontal scale of the perturbations is approximately the Rossby radius ($\sim L_D$) consistent with the theory of baroclinic instability (Pedlosky 1987).

Evidence for the effect of decreasing horizontal scale as the influence of $\mathcal{E}_c$ increases is also apparent in Fig. 5 where $d = 1000$ m. For short optimal growth times ($\tau \sim 1$ day) $\mathcal{E}_c \sim \mathcal{E}_b$, so baroclinic effects are as important as barotropic effects and are manifested as a short horizontal scale. For longer optimal growth times $\mathcal{E}_b \gg \mathcal{E}_c$ in Fig. 5, so baroclinic effects have little influence on the horizontal structure of the perturbations. Similar effects were also noted by Buizza and Palmer (1995) in relation to optimal perturbations in the atmosphere.

The energy released by baroclinic processes generally propagates vertically. To illustrate, Fig. 17 shows contours of the vertical distribution of the horizontally integrated total perturbation energy E at the initial time, and at the optimal growth time (τ), for the fastest growing energy optimals of each basic state in 1990 when $d = 700$ m. At initial time, the maximum in E is located well below the surface at a depth $\sim$800 m. As the optimal perturbations develop and grow, E propagates toward the surface. This aspect of perturbation growth can be understood by considering the conservation of wave-action density of a Rossby wave packet propagating in a slowly varying fluid medium (Bretherton and Garrett 1968; Zeng 1983; Hartmann et al. 1995; Buizza and Palmer 1995). The upstream tilt of streamlines in the vertical (a characteristic signature of energy release by baroclinic processes) is maintained by the competing effects of downstream advection of perturbation vorticity by the basic-state flow and the upstream advection of basic-state vorticity by the perturbation flow. In this way the perturbations are able to sustain energy growth by baroclinic processes.

e. Nonautonomous versus autonomous

To demonstrate the importance of the time history of the basic-state flow on perturbation development, optimal perturbation spectra were computed once every

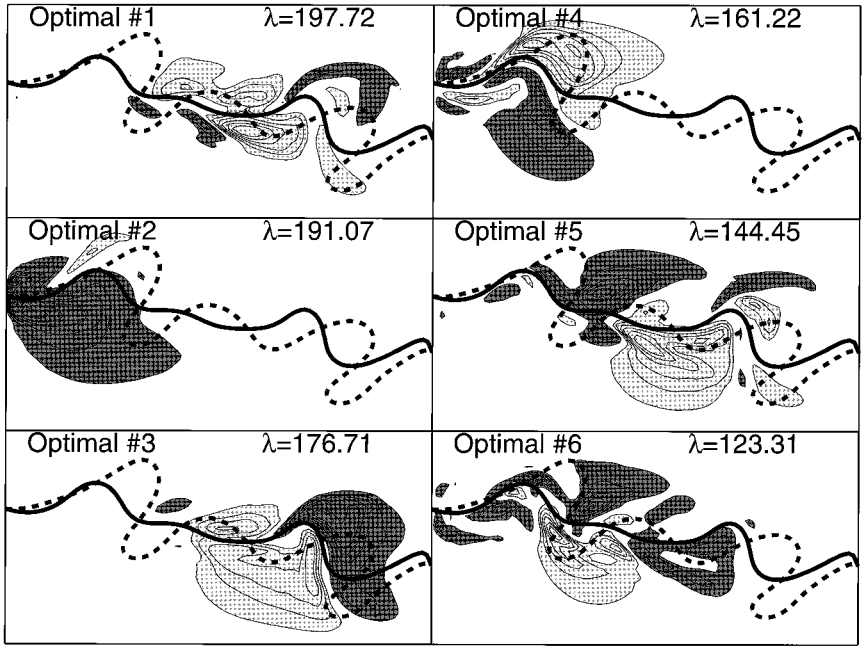

FIG. 13. Maps of surface perturbation stream function $\delta\psi$ for the first six members of the energy optimal spectrum of the time evolving Gulf Stream flow initialized on 1 Jan 1990 (cf. Fig. 2). The optimal growth time $\tau = 8$ days. The perturbation energy growth factor λ is indicated in each case. Light shading indicates where $\delta\psi > 0$ and dark shading where $\delta\psi < 0$. The heavy solid and dashed lines show the position of the Gulf Stream axis at initial time and at the optimal growth time, respectively. The contour interval is arbitrary.

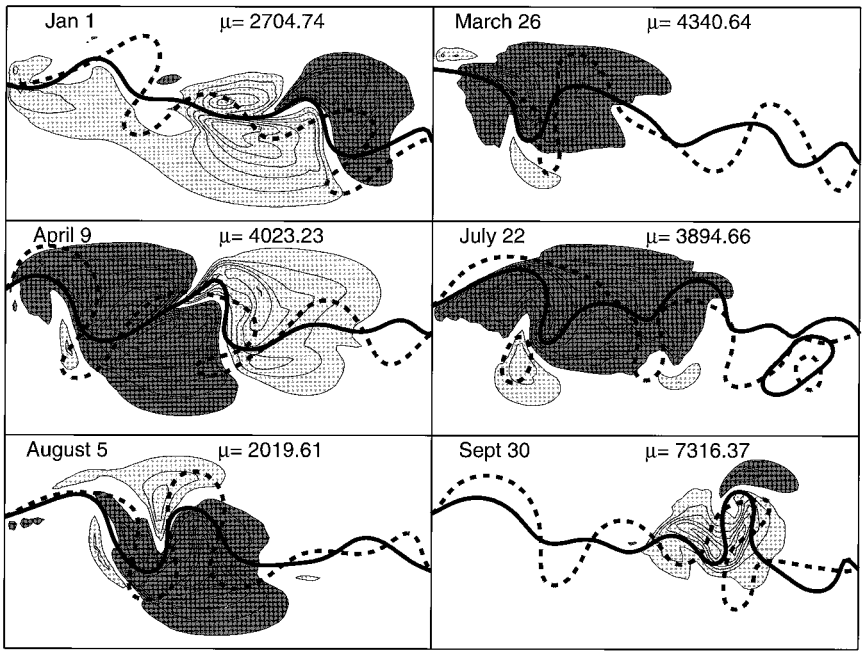

FIG. 14. Maps of surface perturbation potential vorticity $\delta\zeta$ for the fastest growing enstrophy optimals of the time evolving Gulf Stream flows initialized on the dates indicated. The initial configurations of the time evolving Gulf Stream basic state in each case are shown in Fig. 8. The optimal growth time $\tau = 8$ days, and the perturbation enstrophy growth factor μ is indicated in each case. Light shading indicates where $\delta\zeta > 0$ and dark shading where $\delta\zeta < 0$. The heavy solid and dashed lines show the position of the Gulf Stream axis at initial time and at the optimal growth time, respectively. The contour interval is arbitrary.

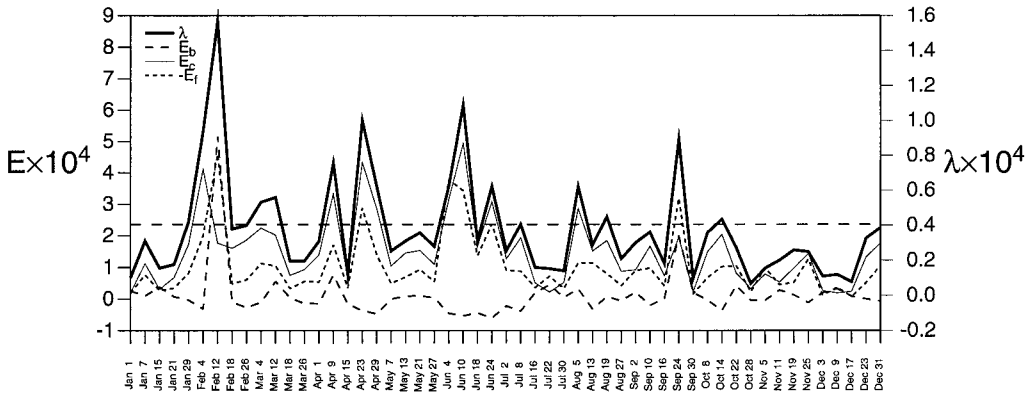

FIG. 15. The energy growth factors λ and perturbation energy components $\mathcal{E}_b$, $\mathcal{E}_c$, and $\mathcal{E}_f$ (in nondimensional units) of the fastest growing members of the optimal perturbation spectra for time evolving basic-state flows initialized on the dates indicated with $d = 700$ m in the feature model (8). In each case the optimal growth time $\tau = 8$ days. The horizontal dashed line shows the annual mean value of λ.

week for the 1990 cases using snapshots of the Gulf Stream as autonomous basic states. These basic states correspond to the initial configurations of the time evolving basic states used in the calculations of Fig. 9. As in sections 4b and 4c, $d = 1000$ m in (8) and $\tau = 8$ days. Figure 18 shows variations in λ throughout the year for the energy optimals of the resulting autonomous basic states. Compared to the nonautonomous case (Fig. 9a), there is much less variation in λ throughout the year. However, Fig. 18 shows that certain stationary basic-state configurations (e.g., 12 Feb, 22 Jul, and 8 Oct) can support very rapidly growing perturbations. The basic states on these days usually possess a steep meander or eddy–Gulf Stream interaction, which is persisted in time for the entire optimal growth time by virtue of the autonomous condition. As discussed in section 4b, such features of the basic state create conditions that are extremely favorable for perturbation growth.

5. The relationship between optimal perturbations and finite-time normal modes

The stability of time evolving flows can be measured in terms of the Lyapunov exponent defined in (4). However, for many dynamical systems of interest, the limit in (4) cannot be practically reached. Therefore for a finite time interval, the stability of a time evolving flow is sometimes assessed by examining the behavior of the eigenvectors of the linear propagator $R(t_1, t_2)$. The eigenvectors of $R(t_1, t_2)$ are sometimes referred to as finite-time normal modes (Frederiksen 1997). If we denote by χ_i, the eigenvectors of $R(t_1, t_2)$, then

$$R(t_1, t_2)\chi_i = \nu_i\chi_i. \tag{11}$$

The eigenvalues ν_i of $R(t_1, t_2)$ and $R^\dagger(t_1, t_2)$ are identical, so

$$R^\dagger(t_1, t_2)\chi_j^\dagger = \nu_j\chi_j^\dagger \tag{12}$$

defines the eigenvectors $\chi_j^\dagger$ of $R^\dagger(t_1, t_2)$. We will refer to χ_i as a finite-time normal mode (FTNM) and $\chi_j^\dagger$ as an adjoint FTNM. Forming the innerproduct of (12) with $\chi_j^\dagger$ and (13) with χ_i and subtracting the result yields

$$(\nu_i - \nu_j)\langle\chi_i, \chi_j^\dagger\rangle = \delta_{i,j}, \tag{13}$$

where $\delta_{i,j}$ is the Kronecker delta function and χ_i and $\chi_j^\dagger$ are normalized appropriately with $|\chi_i| = |\chi_i^\dagger|$. Equation (13) is an expression of the biorthogonality between the FTNMs of $R(t_1, t_2)$ and the adjoint FTNMs of $R^\dagger(t_1, t_2)$.

The significance of the adjoint FTNMs can be appreciated if we consider an arbitrary perturbation Ψ, with unit norm, composed of a linear superposition of the FTNMs, so that

$$\Psi = \sum_i \alpha_i\chi_i. \tag{14}$$

According to (13), the ''projection'' coefficient, α_k, of Ψ on χ_k is given by

$$\alpha_k = \langle\chi_k^\dagger, \Psi\rangle = |\chi_k^\dagger||\Psi|\cos\theta, \tag{15}$$

where θ is the angle that separates $\chi_k^\dagger$ and Ψ in phase space and $\langle\cdots, \cdots\rangle$ is the L2 norm. Choosing $\Psi = \chi_k^\dagger$ maximises α_k, the projection of Ψ onto the kth FTNM, and of all possible norms $\langle\Psi, X\Psi\rangle$, the L2 norm $\langle\Psi, \Psi\rangle$ initially grows most rapidly as χ_k emerges. To maximize the projection of Ψ on χ_k and produce the most rapid transient growth in another norm $\langle\Psi, X\Psi\rangle$, the biorthogonality relation (13) shows that we must choose $\Psi = X^{-1}\chi_k^\dagger$.

To appreciate the relationship between the adjoint FTNMs, $\chi^\dagger$, and the optimal perturbations, $\hat{\varphi}$, we recall that

$$R^\dagger(t_1, t_2)R(t_1, t_2)\hat{\varphi} = \lambda\hat{\varphi}. \tag{16}$$

As $\tau = t_2 - t_1 \to \infty$, the most unstable eigenvectors of $R(t_1, t_2)$ and $R^\dagger(t_1, t_2)$ will emerge from integrations of

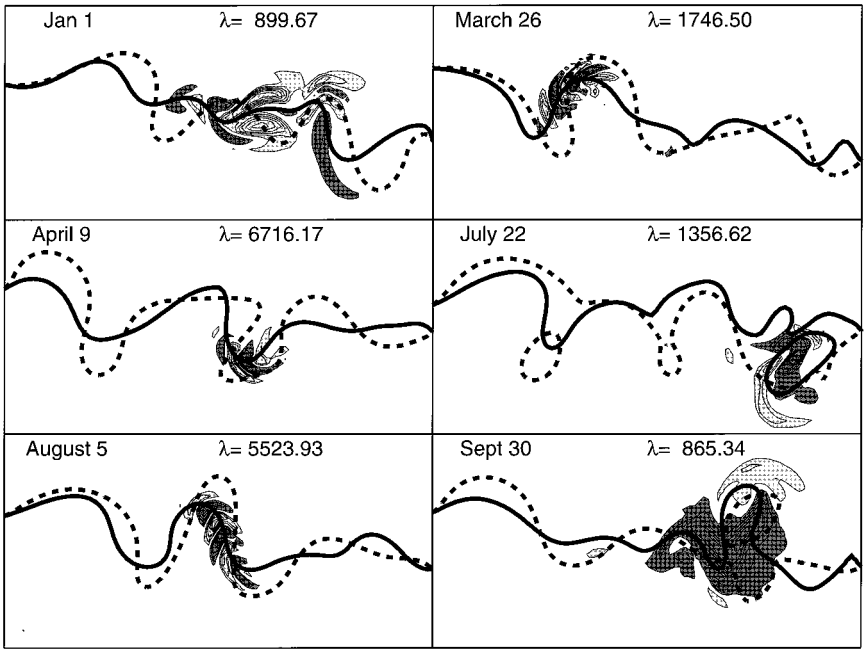

FIG. 16. Maps of surface perturbation stream function $\delta\psi$ before optimal growth for the fastest growing energy optimals of the time evolving Gulf Stream flows on the dates indicated when $d = 700$ m in the feature model described by (8). The optimal growth time $\tau = 8$ days, and the perturbation energy growth factor λ is indicated in each case. Light shading indicates where $\delta\psi > 0$ and dark shading where $\delta\psi < 0$. The heavy solid and dashed lines show the position of the Gulf Stream axis at initial time and at the optimal growth time, respectively. The contour interval is arbitrary.

the tangent linear equation (2) and its adjoint respectively. In other words, $\lim_{\tau\to\infty} R(t_1, t_2)\hat{\varphi} \to \nu\chi$ and so

$$\lim_{\tau\to\infty} R^\dagger(t_1, t_2)R(t_1, t_2)\hat{\varphi} \to R^\dagger(t_1, t_2)(\nu\chi) \to \nu^2\chi^\dagger = \lambda\hat{\varphi}.$$

Therefore according to (16), as $\tau \to \infty$, the structures of the optimal perturbations approach those of the adjoint FTNMs. For the Gulf Stream flows considered in sections 3 and 4, this limit is reached when τ is greater than about 8 days. To illustrate, Fig. 19 shows the real component of $\delta\zeta$ for the fastest growing adjoint FTNM when $t_2 - t_1 = 16$ days for the time evolving basic state in Fig. 2 that was used in the calculations of Fig. 7. In this example the adjoint FTNM is purely real with eigenvalue $\nu = 11.25$. A comparison of Figs. 19 and 7 reveals that for $\tau \sim$14–16 days, the structures of the fastest growing enstrophy optimal perturbations resemble those of the adjoint FTNMs. Evidence of this is also apparent in Fig. 6, which shows that for $\tau >$9 days, the enstrophy optimals all grow at the same rate, which is the growth rate of the fastest growing adjoint FTNM. During the last few days of optimal growth, the enstrophy optimals with optimal growth times $\tau >$9 days grow at a slower rate than they do during their early period of growth, and during the later stages of growth, the growth rate is almost constant. The enstrophy of a perturbation with this constant growth rate would grow by a factor of about 130 in 16 days, as indicated in Fig. 6, which is consistent with the adjoint FTNM in Fig. 19 with an eigenvalue $\nu = 11.25$, corresponding to a growth factor in Q of 126.

To relate the adjoint FTNMs to the energy optimals we must consider the growth of $\mathcal{L}\chi^\dagger$ to produce the most rapid transient growth of the energy norm arising from the adjoint FTNM, where $\mathcal{L} = [\nabla^2 \cdot + \partial/\partial z(S^{-1}\partial/\partial z \cdot)]$. If the initial vorticity structure of $\chi^\dagger$ is as shown in Fig. 19, then the energy norm of $\mathcal{L}\chi^\dagger$ grows by a factor of 5016, which compares favorably with the growth rate of the 16-day energy optimal toward the end of its optimal growth time as shown in Fig. 4. This also explains the similarity between the $\delta\psi$ of the energy optimals in Fig. 5 and the $\delta\zeta$ of the enstrophy optimals in Fig. 7 when $\tau >$ 8 days.

According to (15), the adjoint FTNMs are the optimal excitations for the FTNMs. Therefore, given the correspondence between the structures of the optimal perturbations and the adjoint FTNMs after only a week or so, the optimal perturbations also act as optimal excitations of the FTNMs. If the FTNMs are a good indication (in the limit of linear dynamics) of the most asymptotically unstable directions in phase space of the basic-state flow, then our results show that the optimal perturbations ''rotate'' more rapidly toward these most unstable directions than any other perturbations. This is in agreement with the ideas of Farrell and Ioannou

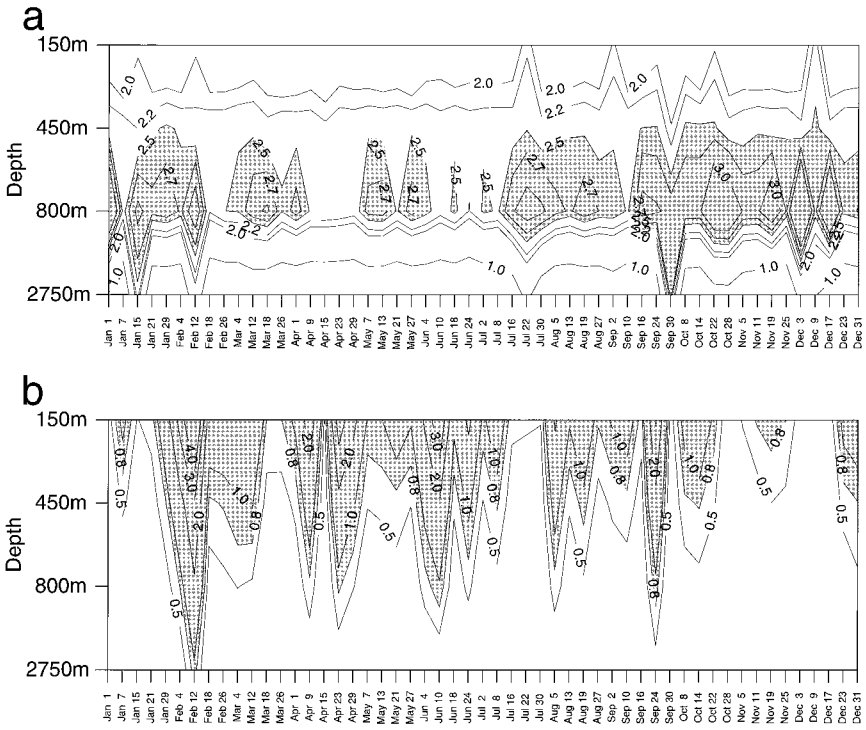

FIG. 17. Contours of the total perturbation energy E as a function of depth for the fastest growing energy optimal of each basic state in 1990: (a) E at the initial time multiplied by 10 and (b) E at the optimal growth time divided by 1000. In (a) shading indicates where $E > 0.25$ and in (b) where $E > 800$. The units of nondimensional energy are arbitrary and the same in (a) and (b).

(1996b). We should note, however, that according to Fig. 10 the tangent linear approximation is not valid for time periods of 16 days unless the perturbation amplitudes are initially very small.

6. Discussion and conclusions

In this study, we have demonstrated that the ideas of generalized linear stability analysis, proposed recently by Farrell and Ioannou (1996a,b), are applicable to complex dynamical flow fields such as we find in the ocean. We have applied these ideas to the Gulf Stream in an attempt to investigate the potential for forecast error growth in ocean model forecasts and so guide us in our approach to ensemble prediction described in Part II. The Gulf Stream flows that we have considered are typical of those we would expect to obtain from forecasts of the system. Our results indicate that there is the po-

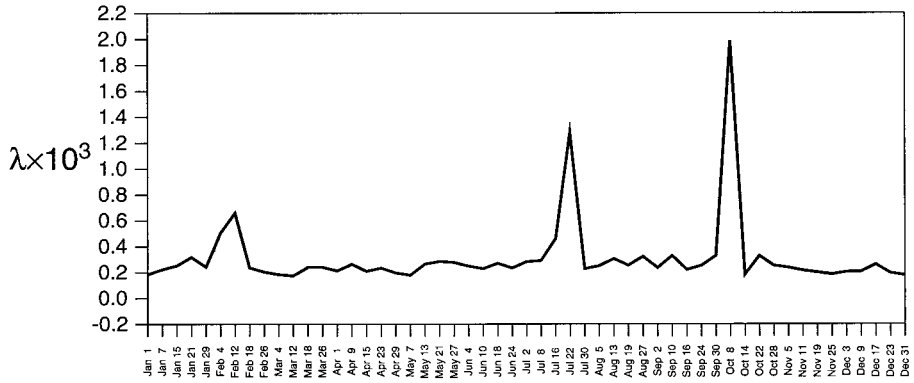

FIG. 18. The energy growth factors λ of the fastest growing members of the energy optimal spectra for autonomous basic states composed of snapshots of the Gulf Stream flow on the dates indicated on the abscissa.

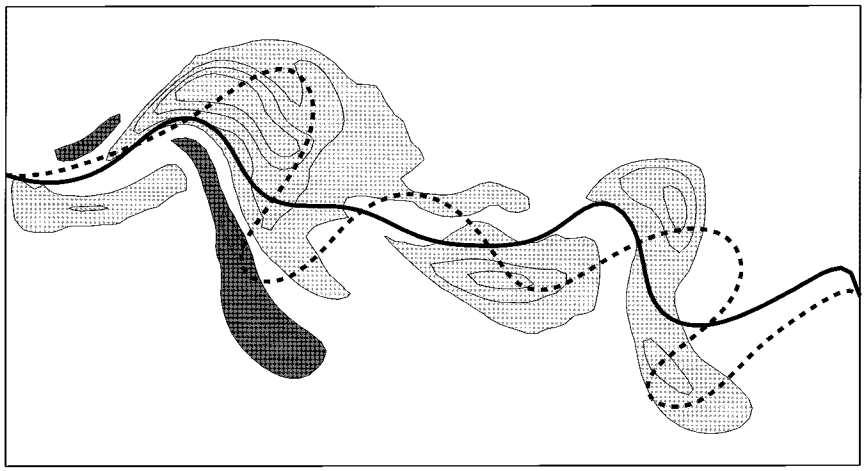

FIG. 19. The real component of the surface perturbation potential vorticity $\delta\zeta$ of the fastest growing adjoint FTNM over 16 days on the time evolving basic state initialized on 1 Jan 1990 (cf. Fig. 2). In this case the adjoint FTNM is purely real. Light shading indicates where $\delta\zeta > 0$ and dark shading where $\delta\zeta < 0$. The heavy solid and dashed lines show the position of the Gulf Stream axis at initial time and at the optimal growth time, respectively. The contour interval is arbitrary.

tential for errors or uncertainties in the initial conditions of such forecasts to be amplified considerably in regions of developing straining and shearing flow. Such regions include developing meanders, regions where eddies form, and where existing eddies interact with the Gulf Stream. If the effects of surface forcing and bathymetry were included, errors and uncertainties in these fields (or the flows resulting from them) would translate into errors in the vertical velocity field w in (7), and these errors could also be amplified. The optimal perturbation calculations of section 4 indicate how, where, and why perturbations and forecast errors can amplify.

We must, however, also consider the development of naturally occuring perturbations in the nature that may not be captured by the model forecast. These perturbations can arise from nonlinearities not captured by the model, from high-frequency noise in the surface forcing not resolved by the observations, as well from high-frequency internal waves generated by bathymetry which are perhaps not resolved by the model grid, or which are filtered out of the model by dynamical constraints (e.g., by quasigeostrophic constraints). Tidal forcing may also be another source of perturbations through their nonlinear interaction with the Gulf Stream and with bathymetry. The potential role of stochastic forcing in the atmosphere and ocean systems has been considered by several authors (e.g., Farrell and Ioannou 1993a,b, 1994, 1996a,b; Kleeman and Moore 1997; Penland 1997; Moore and Kleeman 1999). Whatever the source of the perturbations, it is clear that they can undergo rapid amplification in the same way suggested by the optimal perturbations of section 4. Therefore such perturbations can act as precursors for the rapid development of meanders and eddies in nature. If these precursors are absent from the model, a forecast may be seriously in error. Therefore, any assessment of the predictability of ocean currents such as the Gulf Stream must take into account the presence of noise-induced perturbations in the system. One approach to this problem is ensemble prediction in which a forecast is repeated many times starting from slightly different initial conditions.

The ideas of generalized linear stability theory have been applied successfully to the problem of ensemble prediction in operational numerical weather prediction, where attempts are routinely made to estimate the predictability of the current state of the atmosphere. At ECMWF, each member of an ensemble of forecasts is perturbed using linear combinations of the optimal perturbations of the atmosphere (Molteni et al. 1996), while at NCEP approximations of the FTNMs are used to perturb the forecast system (Tracton and Kalnay 1993; Toth and Kalnay 1993). In each case, the potential predictability of the current state of the atmosphere is assessed in terms of the rate at which the individual ensemble members diverge relative to each other. These same techniques and ideas are also proving useful for estimating the predictability of the El Niño–Southern Oscillation (Moore and Kleeman 1998) and for assessing the predictability of ocean flows such as the Gulf Stream as demonstrated in Part II.

We have found that the optimal perturbations of the Gulf Stream resemble in many ways those of the jet streams in the atmosphere. In addition, ideas and theories for the development of Rossby wave packets in the atmosphere are also applicable to the ocean. This gives us further encouragement that the optimal perturbation-based ensemble prediction techniques being developed in NWP will also prove valuable in primitive-equation ocean general circulation models. The appli-

cation of these same techniques to the primitive-equation ocean will be the subject of a future study.

Acknowledgments. This research was supported by the National Science Foundation, Ocean Sciences Division, by a grant awarded to Andrew Moore (OCE-9696199). Arthur Mariano acknowledges the support of the Office of Naval Research (N00014-95-1-0257). We also acknowledge helpful conversations with Dr. Tim Palmer on this work. Many thanks to Kevin Kohler for help with the figures.

REFERENCES

Bretherton, F. P., and C. J. R. Garrett, 1968: Wavetrains in inhomogeneous moving media. *Proc. Roy. Soc. London A,* **302,** 529–554.

Buizza, R., and T. N. Palmer, 1995: The singular-vector structure of the atmospheric global circulation. *J. Atmos. Sci.,* **52,** 1434–1456.

Charney, J. G., R. Fjortoft, and J. von Neumann, 1950: Numerical integrations of the barotropic vorticity equation. *Tellus,* **2,** 237–254.

Chin, T. M., and A. J. Mariano, 1997: Space–time interpolation of oceanic fronts. *IEEE Trans. Geosci. Remote Sens.,* **35,** 734–746.

Farrell, B. F., 1990: Small error dynamics and the predictability of flows. *J. Atmos. Sci.,* **47,** 2409–2416.

——, and A. M. Moore, 1992: An adjoint method for obtaining the most rapidly growing perturbation to oceanic flows. *J. Phys. Oceanogr.,* **22,** 338–349.

——, and P. J. Ioannou, 1993a: Stochastic forcing of the linearized Navier-Stokes equations. *Phys. Fluids,* **5,** 2600–2609.

——, and ——, 1993b: Stochastic dynamics of baroclinic waves. *J. Atmos. Sci.,* **50,** 4044–4057.

——, and ——, 1994: Variance maintained by stochastic forcing of nonnormal dynamical systems associated with linearly stable shear flows. *Phys. Rev. Lett.,* **72,** 1188–1191.

——, and ——, 1996a: Generalized stability theory. Part I: Autonomous operators. *J. Atmos. Sci.,* **53,** 2025–2040.

——, and ——, 1996b: Generalized stability theory. Part II: Nonautonomous operators. *J. Atmos. Sci.,* **53,** 2041–2053.

Frederiksen, J. S., 1997: Adjoint sensitivity and finite-time normal mode disturbances during blocking. *J. Atmos. Sci.,* **54,** 1144–1165.

Haidvogel, D. B., A. R. Robinson, and E. E. Schulman, 1980: The accuracy, efficiency and stability of three numerical models with application to open ocean problems. *J. Comput. Phys.,* **34,** 1–53.

Hartmann, D. L., R. Buizza, and T. N. Palmer, 1995: Singular vectors: The effect of spatial scale on linear growth of disturbances. *J. Atmos. Sci.,* **52,** 3885–3894.

Holloway, G., and B. J. West, 1984: Predictability of fluid motions. AIP Conf. Proc. No. 106, Amer. Inst. Phys., 612 pp.

Kelvin, 1887: Stability of fluid motions: Rectilinear motion of a viscous fluid between two parallel plates. *Philos. Mag.,* **24,** 188–196.

Kleeman, R., and A. M. Moore, 1997: A theory for the limitations of ENSO predictability due to stochastic atmospheric transients. *J. Atmos. Sci.,* **54,** 753–767.

Lacarra, J. F., and O. Talagrand, 1988: Short range evolution of small perturbations in a barotropic model. *Tellus,* **40A,** 81–95.

Lai, C.-C. A, W. Qian, and S. M. Glenn, 1994: Data Assimilation and Model Evaluation Experiment datasets. *Bull. Amer. Meteor. Soc.,* **75,** 793–809.

Lorenz, E. N., 1965: A study of the predictability of a 28-variable atmospheric model. *Tellus,* **17,** 321–333.

Mariano, A. J., 1990: Contour analysis: A new approach to melding geophysical fields. *J. Atmos. Oceanic Technol.,* **7,** 285–295.

Miller, R. N., A. R. Robinson, and D. B. Haidvogel, 1981: A baroclinic quasi-geostrophic open ocean model. *J. Comput. Phys.,* **50,** 38–70.

Molteni, F., and T. N. Palmer, 1993: Predictability and finite-time instability of the northern winter circulation. *Quart. J. Roy. Meteor. Soc.,* **119,** 269–298.

——, R. Buizza, T. N. Palmer, and T. Petroliagis, 1996: The ECMWF ensemble prediction system: Methodology and validation. *Quart. J. Roy. Meteor. Soc.,* **122,** 73–120.

Moore, A. M., 1991: Data assimilation in a quasigeostrophic open ocean model of the Gulf Stream region using the adjoint method. *J. Phys. Oceanogr.,* **21,** 398–427.

——, 1999: The dynamics of error growth and predictability in a model of the Gulf Stream. Part II: Ensemble prediction. *J. Phys. Oceanogr.,* in press.

——, and B. F. Farrell, 1993: Rapid perturbation growth on spatially and temporally varying oceanic flows determined using an adjoint method: Application to the Gulf Stream. *J. Phys. Oceanogr.,* **23,** 1682–1702.

——, and ——, 1996: The dynamics of error growth and predictability in a coupled model of ENSO. *Quart. J. Roy. Meteor. Soc.,* **122,** 1405–1446.

——, and ——, 1997a: The singular vectors of a coupled ocean–atmosphere model of ENSO. Part I: Thermodynamics, energetics and error growth. *Quart. J. Roy. Meteor. Soc.,* **123,** 953–981.

——, and ——, 1997b: The singular vectors of a coupled ocean–atmosphere model of ENSO. Part II: Sensitivity studies and dynamical interpretation. *Quart. J. Roy. Meteor. Soc.,* **123,** 983–1006.

——, and ——, 1998: Skill assessment for ENSO using ensemble prediction. *Quart. J. Roy. Meteor. Soc.,* **124,** 557–584.

——, and ——, 1999: Stochastic forcing of ENSO by the intraseasonal oscillation. *J. Climate,* in press.

Mureau, R., F. Molteni, and T. N. Palmer, 1993: Ensemble prediction using dynamically conditioned perturbations. *Quart. J. Roy. Meteor. Soc.,* **119,** 299–323.

Orr, W. M., 1907: Stability or instability of the steady motions of a perfect liquid. *Proc. Roy. Irish. Acad.,* **27,** 9–69.

Pedlosky, J., 1987: *Geophysical Fluid Dynamics*. 2d ed. Springer-Verlag, 710 pp.

Penland, M. C., 1996: A stochastic model of IndoPacific sea surface temperature anomalies. *Physica D,* **98,** 534–558.

Raleigh, J. W. S., 1880: On the stability, or instability, of certain fluid motions. *Proc. London Math. Soc.,* **9,** 57–70.

Robinson, A. R., M. A. Spall, and N. Pinardi, 1988: Gulf Stream simulations and the dynamics of ring and meander processes. *J. Phys. Oceanogr.,* **18,** 1811–1853.

——, ——, L. J. Walstad, and W. G. Leslie, 1989a: Data assimilation and dynamical interpolation in GULFCAST experiments. *Dyn. Atmos. Oceans,* **13,** 301–316.

——, S. M. Glenn, M. A. Spall, L. J. Walstad, G. M. Gardiner, and W. G. Leslie, 1989b: Forecasting Gulf Stream meanders and rings. *Eos, The Oceanography Report,* **70** (45), 1464–1473.

Shapiro, R., 1970: Smoothing, filtering and boundary effects. *Rev. Geophys. Space Phys.,* **8,** 359–386.

Spall, M. A., and A. R. Robinson, 1990: Regional primitive equation studies of the Gulf Stream meander and ring formation. *J. Phys. Oceanogr.,* **20,** 985–1016.

Sorensen, D. C., 1992: Implicit application of polynomial filters in a k-step Arnoldi method. *SIAM J. Matrix Anal. Appl.,* **13,** 357–385.

Toth, Z., and E. Kalnay, 1993: Ensemble prediction at NMC: The generation of perturbations. *Bull. Amer. Meteor. Soc.,* **74,** 2317–2330.

Tracton, M. S., and E. Kalnay, 1993: Operational ensemble prediction at the National Meteorological Center: Practical aspects. *Wea. Forecasting,* **8,** 379–398.

Watts, D. R., and W. E. Johns, 1982: Gulf Stream meanders: Observations of propagation and growth. *J. Geophys. Res.,* **87,** 9467–9476.

Willems, R. C., and Coauthors, 1994: Experiment evaluates ocean models and data assimilation in the Gulf Stream. *Eos, Trans. Amer. Geophys. Union,* **75,** 385.

Zeng, Q.-C., 1983: The evolution of a Rossby-wave packet in a three-dimensional baroclinic atmosphere. *J. Atmos. Sci.,* **40,** 73–84.